A Journal of the Gesellschaft Deutscher Chemiker

Angewandte International Edition Chemie

GDCh

www.angewandte.org

Accepted Article

Title: Compressive Strain Modulation of Single Iron Sites on Helical Carbon Support Boosts Electrocatalytic Oxygen Reduction

Authors: Yuen Wu, Jia Yang, Zhiyuan Wang, Chun-Xiang Huang, Yida Zhang, Qinghua Zhang, Cai Chen, Junyi Du, Xiao Zhou, Ying Zhang, Huang Zhou, Lingxiao Wang, Xusheng Zheng, Lin Gu, and Li-Ming Yang

To be cited as: *Angew. Chem. Int. Ed.* 10.1002/anie.202109058

Link to VoR: https://doi.org/10.1002/anie.202109058

WILEY-VCH

10.1002/anie.202109058

COMMUNICATION

WILEY-VCH

Compressive Strain Modulation of Single Iron Sites on Helical Carbon Support Boosts Electrocatalytic Oxygen Reduction

Jia Yang,[a,b,§] Zhiyuan Wang,[b,§] Chun-Xiang Huang,[c,§] Yida Zhang,[d] Qinghua Zhang,[e] Cai Chen,[b] Junyi Du,[b] Xiao Zhou,[b] Ying Zhang,[b] Huang Zhou,[b] Lingxiao Wang,[b] Xusheng Zheng,*[d] Lin Gu,[e] Li-Ming Yang,*[c] Yuen Wu*[b]

[a] Dr. J. Yang
Institutes of Physical Science and Information Technology, Key Laboratory of Structure and Functional Regulation of Hybrid Materials of Ministry of Education, Anhui Graphene Engineering Laboratory
Anhui University
Hefei, Anhui 230601, China

[b] Dr. J. Yang, Dr. Z. Wang, C. Chen, Dr. J. Du, Dr. X. Zhou, Dr. Y. Zhang, Dr. H. Zhou, L. Wang, Prof. Y. Wu
Hefei National Laboratory for Physical Sciences at the Microscale, Collaborative Innovation Center of Chemistry for Energy Materials (iChEM), School of Chemistry and Materials Science
University of Science and Technology of China
Hefei, Anhui 230026, China
E-mail: yuenwu@ustc.edu.cn

[c] C.-X. Huang, Prof. L.-M. Yang
Hubei Key Laboratory of Bioinorganic Chemistry and Materia Medica, Key Laboratory of Material Chemistry for Energy Conversion and Storage of Ministry of Education, Hubei Key Laboratory of Materials Chemistry and Service Failure, Hubei Engineering Research Center for Biomaterials and Medical Protective Materials, School of Chemistry and Chemical Engineering
Huazhong University of Science and Technology
Wuhan, Hubei 430074, China
E-mail: Lmyang.uio@gmail.com, Lmyang@hust.edu.cn

[d] Y. Zhang, Prof. X. Zheng
National Synchrotron Radiation Laboratory (NSRL)
University of Science and Technology of China
Hefei, Anhui 230029, China
E-mail: zxs@ustc.edu.cn

[e] Dr. Q. Zhang, Prof. L. Gu
Beijing National Laboratory for Condensed Matter Physics
Institute of Physics, Chinese Academy of Sciences
Beijing 100190, China

[§] J. Yang, Z. Wang, C. Huang contribute equally

Abstract: Designing and modulating the local structure of metal sites is the key to gain the unique selectivity and high activity of single metal site catalysts. Herein, we report strain engineering of curved single atomic iron-nitrogen sites to boost electrocatalytic activity. First, a helical carbon structure with abundant high-curvature surface is realized by carbonization of helical polypyrrole that is templated from self-assembled chiral surfactants. The high-curvature surface introduces compressive strain on the supported Fe-N_4 sites. Consequently, the curved Fe-N_4 sites with 1.5% compressed Fe-N bonds exhibit downshifted d-band center than the planar sites. Such a change can weaken the bonding strength between the oxygenated intermediates and metal sites, resulting a much smaller energy barrier for oxygen reduction. Catalytic tests further demonstrate that a kinetic current density of 7.922 mA/cm^2 at 0.9 V *vs.* RHE is obtained in alkaline media for curved Fe-N_4 sites, which is 31 times higher than that for planar ones. Our findings shed light on modulating the local three-dimensional structure of single metal sites and boosting the catalytic activity via strain engineering.

Single metal site catalysts, with isolated single metal sites dispersed on proper supports, have been emerging as a new frontier in material and catalysis science.[1,2] They integrate the advantages of homogeneous and heterogeneous catalysts such as maximum atomic utilization efficiency, quantum-size effect and tunable electronic environment, thus exhibiting ultra high activity and unique selectivity in various catalytic reactions.[3-13] Among which, carbon support single metal site catalysts with atomic metal-nitrogen sites are promising candidates for energy related catalytic reactions.[4,10]

To further improve or regulate the catalytic activity of carbon supported single metal site catalysts (M-N_x/C), various strategies have been developed.[14] Considering that the catalytic activity of the metal sites is closely related with the coordination structure, numerous efforts are devoted to engineering the coordination numbers, coordinated atoms, environmental atoms, axial guest groups and etc. to tune the intrinsic activity and selectivity of the metal sites for desired applications.[15] However, the above strategies are mainly focused on the in-plane structure of metal-nitrogen sites. The local three-dimensionally structural modulation on the metal sites, which could mediate the catalytic activity by strain effect, still remains challenging and has rarely been discussed.[16] The local three-dimensional structure of metal sites is highly correlated with the surface morphology and geometric structure of support.[17] Compared with the flat surface, high-curvature surface tends to create nonplanar curved structure and introduce strain effect, which may be benificial to improving the catalytic activity.[18] Single metal sites could also be immobilized stronger on high-curvature support, affecting the catalytic activity.[19-22]

Herein, we report strain engineering of curved single atomic iron-nitrogen sites to boost electrocatalytic activity for oxygen reduction reaction (ORR). Helical polypyrrole is firstly obtained by using self-assembled chiral surfactants as the polymerization template. After pyrolysis, right-handed helical single atomic iron catalyst (D-Fe SAC) is obtained, featuring with isolated Fe-N_4 sites on helical high-curvature hollow carbon nanofibers. The high-curvature surface introduces compressive strain effect on the supported Fe-N_4 sites. As a result, the D-Fe SAC delivers

higher activity for ORR compared with the non-helical LD-Fe SAC. Theoretical calculations reveal that the curved structure and compressive strain could regulate the electronic state of Fe-N_4 sites, and further reduce the energy barrier for ORR. Addtionally, various curved metal-nitrogen sites were also obtained based on other metal elements (e.g., Co and Ni). Our research provides insights on modulating the local three-dimensional structure of single metal sites and boosting the catalytic activity via strain engineering.

Figure 1a illustrates the synthesis process of the helical single atomic iron catalyst. Stearol chloride was reacted with D-glutamic acid to give chiral surfactant N-stearoyl-D-glutamic acid. The chiral surfactants underwent a self-assembly process to form helical micelles, which were further used as the templates for pyrrole polymerization.[23] The obtained D-polypyrrole shows a right-handed helical morphology, as demonstrated by the scanning electron microscopy (SEM) and transmission electron microscopy (TEM) images (Figure S1). Taking advantage of the interaction between the empty d orbitals of metal ions and the lone electron pairs of nitrogen atoms on polypyrrole, iron species can be introduced into D-polypyrrole.[24] The iron containing D-polypyrrole was then pyrolyzed under inert atmosphere to afford D-Fe SAC. Metal free D-PPy-Carbon was obtained by pyrolyzing D-polypyrrole. At the same time, the orientation of the helical morphology can be modulated. L-Fe SAC with left-handed helical morphology was obtained from N-stearoyl-L-glutamic acid (Figure S2 and S3). LD-Fe SAC was prepared from non-chiral surfactant N-stearoyl-L/D-glutamic acid. Hollow tubular structures without helical morphology are observed for LD-Fe SAC (Figure S4).

No characteristic peaks ascribed to iron related crystalline species can be identified from the powder X-ray diffraction (PXRD) patterns (Figure S5), and the broad peaks locating at c.a. 26 degree are ascribed to carbon. This indicates that the polypyrrole precursor is successfully transformed into carbon-based material without the formation of crystalline iron species.[25] Representative defective (1353 cm^{-1}) and graphitic bands (1590 cm^{-1}) of pyrolytic carbon can be seen in Raman spectra (Figure S6).[26] Nitrogen sorption isotherms (Figure S7) could be classified into the type IV isotherm.[27] The steep gas uptake at low pressure, together with the hysteresis loop, reveals the micro and meso-porous nature of the carbon material, which is also confirmed by pore size distribution results.

Right-handed helical morphology is retained for D-Fe SAC after pyrolysis, which is confirmed by SEM and TEM images (Figure 1b and 1c). No metal particles are visible in the TEM images (Figure 1c and 1d). Elemental mapping results (Figure 1e) reveal that iron and nitrogen are homogeneously dispersed throughout the carbon matrix. The bright dots with approximately 0.14 nm size in the aberration-corrected high-angle annular dark-field scanning transmission electron microscopy (HAADF-STEM) images reveal that iron disperse as isolated single sites on the carbon support (Figure 1f).[28] Moreover, it can be clearly observed that the helical morphology results in the edge curving of the hollow nanofibers, creating abundant high-curvature carbon lattices (Figure 1g). Consequently, large quantities of single Fe sites are located in the high-curvature carbon lattices (Figure 1f, 1g and S8). In contrast, no high-curvature carbon lattices are observed for LD-Fe SAC. Single Fe sites are

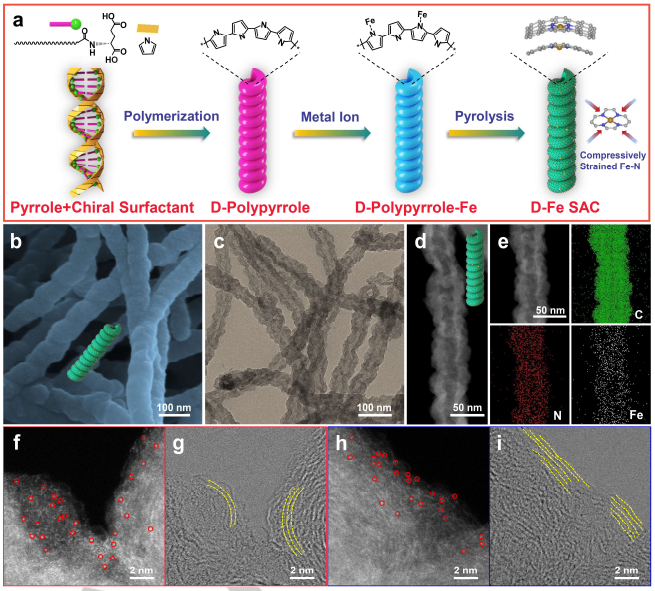

Figure 1. (a) Schematic showing the synthesis process of D-Fe SAC. (b) SEM image, (c) TEM image, (d) HAADF-STEM image, (e) elemental mapping images of D-Fe SAC. (f-i) Aberration-corrected HAADF-STEM images of D-Fe SAC (f, g) and LD-Fe SAC (h, i).

distributed in the straight flat carbon lattices (Figure 1h, 1i, S9 and S10).

The iron content in D-Fe SAC is 1.6 wt% by inductively coupled plasma-mass spectroscopy (ICP-MS) measurement. X-ray photoelectron spectroscopy (XPS) spectra were taken to investigate the surface states of the D-Fe SAC. Peaks assigning to carbon, nitrogen and iron are observed in the XPS full scan spectrum (Figure S11 and 2a). The C 1s spectrum and fitting results reveal the existence of carbon-nitrogen species on the support.[29] Pyridinic N, pyrrolic N, graphitic N and oxidized N are distinguished in N 1s spectrum.[30,31] The fitted Fe $2p_{3/2}$ spectrum reveals that iron exists in ionic state with an oxidation state between 0 and +3.[32,33] The iron content in LD-Fe SAC is 1.67 wt%. The PXRD pattern, Raman spectrum, nitrogen sorption isotherm and XPS spectra of LD-Fe SAC (Figure S5, S6, S7 and S12) indicate that LD-Fe SAC is similar to D-Fe SAC in aspects of the iron loading, crystalline degree, graphitic degree, surface area, pore size distribution and surface chemical states.

The fine structure of Fe species was clarified by X-ray absorption near edge spectra (XANES) and extended X-ray absorption fine structure spectra (EXAFS). The absorption edge in Fe K-edge XANES of D-Fe SAC locates between Fe foil and Fe_2O_3 (Figure 2b), in accordance with the Fe 2p XPS analysis (Figure S11). In the Fourier Transformed (FT) EXAFS of D-Fe SAC, the peak at ~1.4 Å is ascribed to the Fe-N interaction, and no peaks assigning to Fe-Fe interaction are observed (Figure 2c).[34,35] These results agree with the Wavelet Transform analysis, in which only the intensity maximum due to Fe-N interaction is observed for D-Fe SAC (Figure 2d).[36,37] The above results reveal that Fe species are atomically dispersed. Further EXAFS fitting was performed to clarify the coordination structure. The EXAFS fitting using Fe-N_4 in a curved configuration matches well with the experimental result for D-Fe SAC (Figure 2e and Table S1). In contrast, the iron sites in LD-Fe SAC are atomically dispersed with configuration of planar Fe-N_4 (Figure 2b-2e and Table S1). Compared to LD-Fe SAC, the

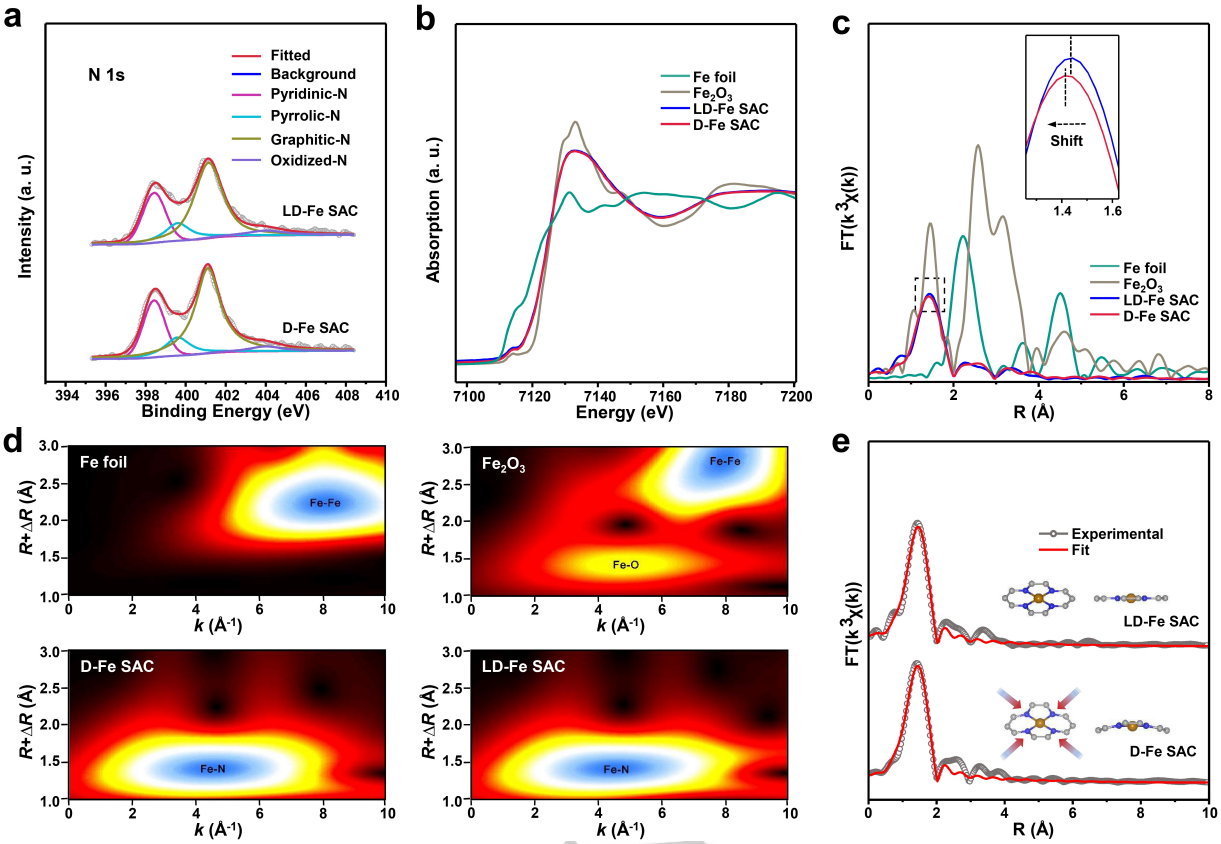

Figure 2. (a) N 1s XPS spectra of D-Fe SAC and LD-Fe SAC. (b) Fe K-edge XANES spectra, (c) FT-EXAFS spectra, (d) Wavelet Transform results of D-Fe SAC, LD-Fe SAC, Fe foil and Fe_2O_3. (e) EXAFS fitting results of D-Fe SAC and LD-Fe SAC.

Fe-N bonds in D-Fe SAC are shortened by about 1.5%, suggesting the compressive strain on Fe-N bonds created by the curved structure. The XANES and EXAFS results demonstrate that isolated Fe-N_4 sites with curved structure and compressive strain are successfully realized in D-Fe SAC.

The electrocatalytic activity of D-Fe SAC toward ORR was then investigated. ORR activity was first investigated in 0.1 M KOH and the linear sweep voltammetric (LSV) curves are shown in Figure 3a. The D-Fe SAC exhibits an outstanding activity with an onset potential (E_{onset}) of 1.015 V *vs.* RHE and a half-wave potential ($E_{1/2}$) of 0.91 V *vs.* RHE. The E_{onset} and $E_{1/2}$ of D-Fe SAC are more positive than those of platinum/carbon (Pt/C, 20 wt%, E_{onset}: 1.013 V *vs.* RHE and $E_{1/2}$: 0.87 V *vs.* RHE). L-Fe SAC exhibits comparable activity to D-Fe SAC with $E_{1/2}$ of 0.9 V *vs.* RHE (Figure S13). The ORR activity of non-helical LD-Fe SAC and metal-free D-PPy-Carbon (Figure S14) was also examined. The E_{onset} and $E_{1/2}$ of LD-Fe SAC are 0.921 V and 0.81 V *vs.* RHE, which are more negative than those of D-Fe SAC. Electrochemical active surface area (ECSA) measurement results indicate that the ECSA of D-Fe SAC and LD-Fe SAC are nearly the same (Figure S15). The LSV curves normalized by Fe loading reveal that D-Fe SAC exhibits higher mass activity than LD-Fe SAC (Figure S16). These highlight the critical role of the curved structure and the compressive strain in achieving the ultra high activity of D-Fe SAC. For D-PPy-Carbon, the E_{onset} and $E_{1/2}$ are 0.86 V and 0.735 V *vs.* RHE, indicating that iron play a vital role in ORR. The electron transfer number during ORR catalyzed by D-Fe SAC is estimated to be 3.96, as calculated from the LSV curves at different rotating speeds and Koutechy-Levich (K-L) plots (Figure S17). The Tafel slope of D-Fe SAC (60 mV/dec) is lower than those of LD-Fe SAC (74 mV/dec) and Pt/C (71 mV/dec), indicating faster kinetics (Figure 3b).[38] The peroxide yields and electron transfer numbers were also investigated by rotating ring-disk electrode (RRDE) measurements. The peroxide yields catalyzed by D-Fe SAC maintain at below 2% and the electron transfer numbers are close to 4 (Figure 3c). These results indicate that D-Fe SAC can efficiently catalyze four-electron ORR under alkaline condition.

The kinetic current densities of the catalysts at 0.9 V *vs.* RHE are shown in Figure 3d. D-Fe SAC exhibits a kinetic current density of 7.922 mA/cm^2, which is vastly enhanced compared with LD-Fe SAC (0.25 mA/cm^2), D-PPy-Carbon (0.029 mA/cm^2) and Pt/C (2.8 mA/cm^2). The kinetic current density of D-Fe SAC at 0.9 V *vs.* RHE is 31 times higher than that of LD-Fe SAC and ranks among the highest values in literatures (Table S2). Methanol tolerance was investigated by introducing methanol during ORR. Negligible current density change occurs for D-Fe SAC, while a sharp current density drop occurs for Pt/C (Figure 3e). The stability of D-Fe SAC for ORR was investigated. No obvious shift of the LSV curve can be observed after 10000 cyclic voltammetric scans (Figure 3f). These results indicate that D-Fe SAC exhibit high activity and stability for ORR in alkaline electrolyte.

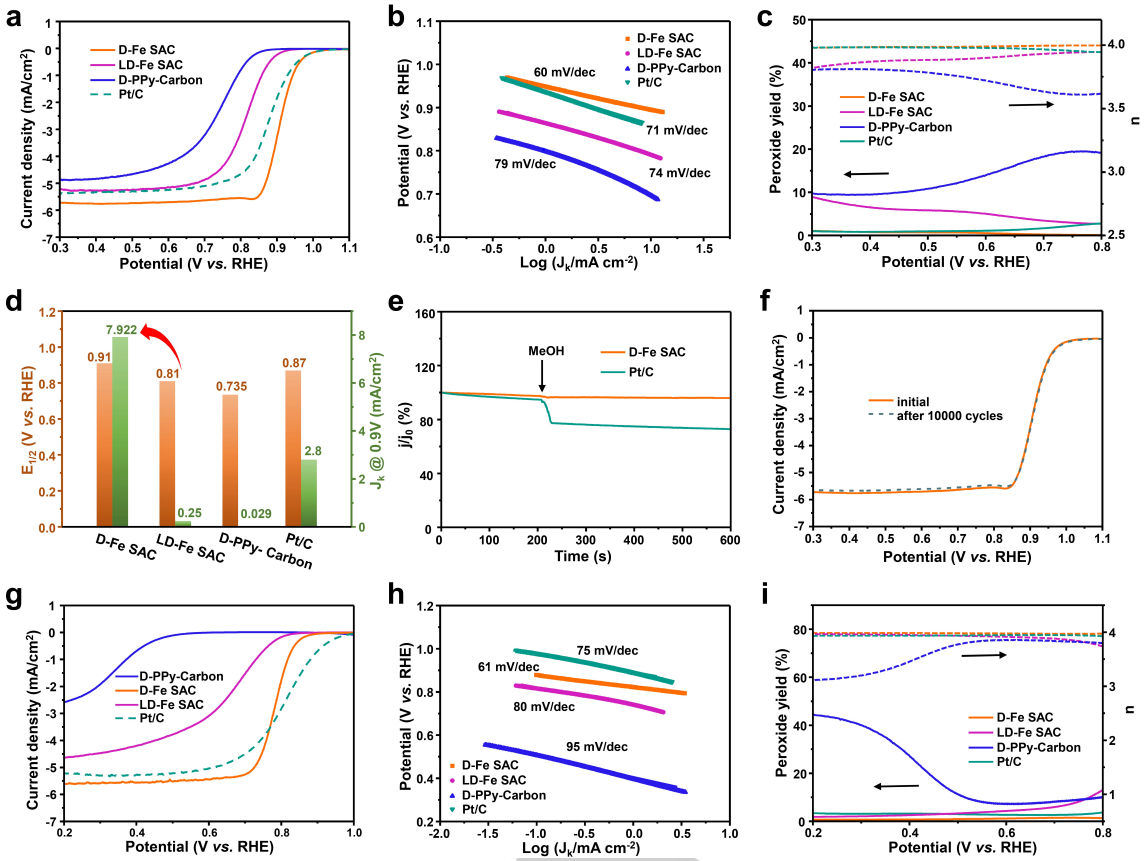

Figure 3. (a) LSV curves, (b) Tafel plots, (c) peroxide yields and electron transfer numbers of D-Fe SAC, LD-Fe SAC, D-PPy-Carbon and Pt/C in 0.1M KOH. (d) Half-wave potentials and kinetic current densities (0.9 V *vs.* RHE) of the catalysts. (e) Methanol tolerance, (f) stability measurement result of D-Fe SAC in 0.1M KOH. (g) LSV curves, (h) Tafel plots, (i) peroxide yields and electron transfer numbers of D-Fe SAC, LD-Fe SAC, D-PPy-Carbon and Pt/C in 0.1M $HClO_4$.

The ORR activity of D-Fe SAC in acidic electrolyte was also examined. LSV measurement of D-Fe SAC in 0.1M $HClO_4$ reveals an $E_{1/2}$ value of 0.78 V *vs.* RHE (Figure 3g). This value is comparable with that of Pt/C (0.8 V *vs.* RHE), and higher than that of LD-Fe SAC (0.66 V *vs.* RHE). The Tafel slope (Figure 3h) of D-Fe SAC (61 mV/dec) is lower than that of LD-Fe SAC (80 mV/dec). The electron transfer number catalyzed by D-Fe SAC is calculated to be 3.98 (Figure S18). The peroxide yields maintain below 1.5% and the electron transfer numbers are close to 4 for D-Fe SAC (Figure 3i), indicating that D-Fe SAC can efficiently realize four-electron ORR in acidic electrolyte (Table S3). The stability measurement result reveal the high stability of D-Fe SAC in acidic electrolyte with $E_{1/2}$ loss of 24mV after 10000 cycles (Figure S19).

The practical application of D-Fe SAC for ORR was further demonstrated in zinc-air battery (Figure 4a).[39] The zinc-air battery using D-Fe SAC as cathodic catalyst can deliver an open circuit potential of 1.52 V, which is higher than those of LD-Fe SAC (1.44 V) and Pt/C (1.49 V). Figure 4b inset shows a LED panel lightened by three zinc-air batteries connected in series. Polarization curves and corresponding power densities (Figure 4c) reveal that D-Fe SAC delivers higher output voltages and power densities than LD-Fe SAC and Pt/C at the same discharge current densities. A maximum power density of 215 mW/cm^2 is achieved at 338 mA/cm^2 current density by D-Fe SAC, which is higher than those by LD-Fe SAC (123 mW/cm^2) and Pt/C (135 mW/cm^2). Galvanostatic discharge curves (Figure 4d) indicate that D-Fe SAC delivers higher output voltage (1.2 V) and specific capacity (785 mAh/g) than LD-Fe SAC (1.09 V, 705 mAh/g) and Pt/C (1.16 V, 770 mAh/g). Using D-Fe SAC as

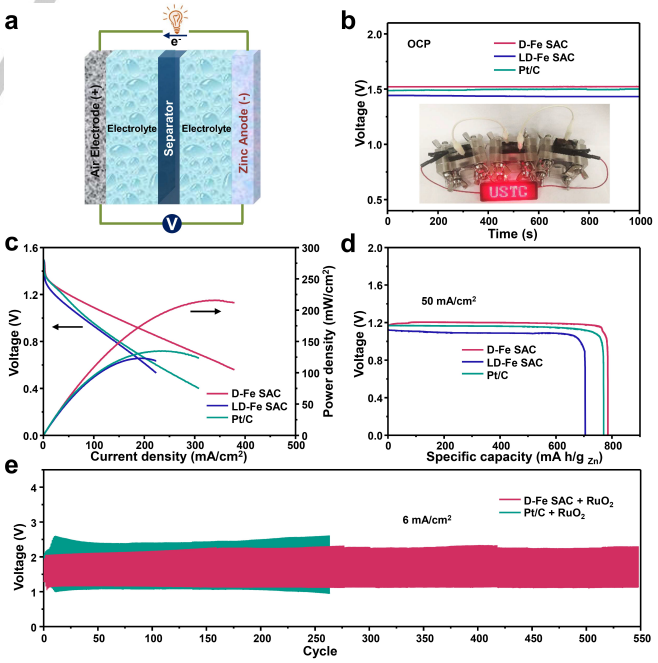

Figure 4. (a) Schematic of zinc-air battery. (b) Open circuit potential curves, (c) polarization curves, (d) discharge curves using D-Fe SAC, LD-Fe SAC and Pt/C as cathodic catalysts. (e) Charge-discharge curves of rechargeable zinc-air batteries using D-Fe SAC and Pt/C as cathodic catalysts.

cathodic catalyst and RuO_2 as anodic catalyst, the rechargeable zinc-air battery can be steadily charge-discharged. The voltage gaps between charge and discharge remain nearly unchanged after 550 cycles, while the obviously voltage gap increases are observed for Pt/C+RuO_2 (Figure 4e). The above results unambiguously reveal the excellent activity and stability of D-Fe SAC as cathodic catalyst in zinc-air battery.

Density functional theory (DFT) calculations were carried out to gain deeper insights into the structure-activity relationship of the curved Fe-N_4 in D-Fe SAC. Models for curved and planar Fe-N_4 are constructed according to the structures resolved by XANES and EXAFS. The planar Fe-N_4 is confined in flat graphene, while the curved Fe-N_4 is built in high-curvature graphene with 1.5% compressed Fe-N bonds. The charge density difference diagrams clearly show the charge transfer from the central Fe to the adjacent N atoms (Figure 5a and 5b). The Bader charge of Fe in curved Fe-N_4 (1.13 e) is larger than that in planar Fe-N_4 (1.08 e), demonstrating a more obvious charge transfer.[40] Additionally, the projected density of states (PDOS) analysis show that the d-band center of curved Fe-N_4 (-1.25 eV) (Figure 5d) is downshifted compared to that of planar Fe-N_4 (-1.18 eV) (Figure 5c), indicating that the adsorption of intermediates are weakened.[41] As a result, the overly strong bonding of the oxygenated intermediates to the Fe sites, which is the main reason that restricts the intrinsic ORR activity of Fe-N_4 sites, is avoided for curved Fe-N_4 sites.[41]

The Gibbs free energy changes of the optimized intermediate species $*O_2$, *OOH, *O, and *OH on the Fe-N_4 sites are shown in Figure 5e, 5f, S20 and S21.[42,43] The potential determination step (PDS) of planar Fe-N_4 for ORR is *OH + $3OH^- + e^- \rightarrow * + 4OH^-$, showing an onset potential of -0.15 V. However, the PDS of curved Fe-N_4 is $*O_2 + 2H_2O + 4e^- \rightarrow$ *OOH + $OH^- + H_2O + 3e^-$, showing an onset potential of -0.10 V (Figure 5e and 5f). Obviously, the ORR onset potential on curved Fe-N_4 is more positive than that on planar Fe-N_4, indicating that curved Fe-N_4 exhibit higher activity than planar Fe-N_4.[44] In short, theoretical calculation results reveal that curved Fe-N_4 sites with compressive strain effect exhibit higher intrinsic activity for ORR compared to planar Fe-N_4 sites.

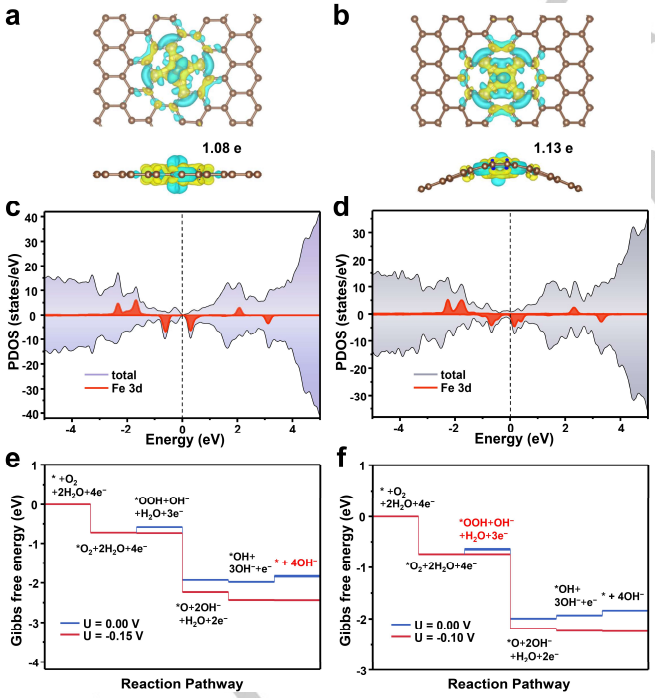

Figure 5. (a, b) Charge density difference diagrams (yellow: electron accumulation, cyan: electron depletion), (c, d) projected density of states, (e, f) ORR Gibbs free energy changes of planar Fe-N_4 (a, c, e) and curved Fe-N_4 (b, d, f).

The versatility of our strategy for fabricating curved metal-nitrogen sites was demonstrated with other metals (e.g., Co and Ni, Table S4). From the PXRD patterns, HAADF-STEM images and elemental mapping images, the homogeneous distribution of Co and Ni sites on helical high-curvature carbon could be identified as isolated single sites (Figure S22-S26). The diversity of helical high-curvature single metal site catalysts might offer powerful tools to advance the developments in chiral catalysis, task-specific sensing, molecule recognition/seperation and etc.

In summary, strain engineering of curved single atomic iron-nitrogen sites to boost electrocatalytic ORR activity is illustrated. The curved Fe-N_4 with compresssive strain exhibit enhanced activity for ORR compared to planar Fe-N_4. Furthermore, the application in zinc-air battery demonstrates a superior ORR performance. DFT calculations reveal that the enhanced activity of curved Fe-N_4 can be attributed to the downshifted d-band center, which optimize the bonding strength towards oxygenated intermediates. This study presents an effective approach to modulate the local structure of single metal sites and boost the catalytic activity via strain engineering. Furthermore, it potentially advances the applications of single metal site catalysts in other chemical and biological fields.

Acknowledgements

This work was supported by China Ministry of Science and Technology (2020YFA0710200), National Key R&D Program of China 2017YFA (0208300, 0700104, 0402904), the National Natural Science Foundation of China (21671180, 22073033, 21873032, 21673087), the DNL Cooperation Fund, CAS (DNL201918), the Fundamental Research Funds for the Central Universities (WK2060120004, WK2060000021, WK2060000025, KY2060000180, 2019kfyRCPY116). The authors thank the photoemission endstations BL1W1B in Beijing Synchrotron Radiation Facility (BSRF), BL14W1 in Shanghai Synchrotron Radiation Facility (SSRF), BL10B and BL11U in National Synchrotron Radiation Laboratory (NSRL), and the Innovation and Talent Recruitment Base of New Energy Chemistry and Device (B21003) for the help in characterizations. The computing work is supported by the public computing service platform provided by Network and Computing Center of HUST.

Keywords: single metal site catalyst • Fe-N-C • curved • strain engineering • oxygen reduction reaction

[1] A. Beniya, S. Higashi, *Nat. Catal.* **2019**, *2*, 590-602.
[2] A. K. Datye, H. Guo, *Nat. Commun.* **2021**, *12*, 895.
[3] X. Li, H. Rong, J. Zhang, D. Wang, Y. Li, *Nano Res.* **2020**, *13*, 1842-1855.
[4] M. B. Gawande, P. Fornasiero, R. Zbořil, *ACS Catal.* **2020**, *10*, 2231-2259.
[5] X. Li, Y. Huang, B. Liu, *Chem* **2019**, *5*, 2733-2739.

[6] J. Liang, J. Lin, J. Liu, X. Wang, T. Zhang, J. Li, *Angew. Chem. Int. Ed.* **2020**, *59*, 12868-12875.

[7] C. Zhu, Q. Shi, S. Feng, D. Du, Y. Lin, *ACS Energy Lett.* **2018**, *3*, 1713-1721.

[8] Z. Jakub, J. Hulva, M. Meier, R. Bliem, F. Kraushofer, M. Setvin, M. Schmid, U. Diebold, C. Franchini, G. S. Parkinson, *Angew. Chem. Int. Ed.* **2019**, *58*, 13961-13968.

[9] X. He, Q. He, Y. Deng, M. Peng, H. Chen, Y. Zhang, S. Yao, M. Zhang, D. Xiao, D. Ma, B. Ge, H. Ji, *Nat. Commun.* **2019**, *10*, 3663.

[10] J. Li, S. Chen, N. Yang, M. Deng, S. Ibraheem, J. Deng, J. Li, L. Li, Z. Wei, *Angew. Chem. Int. Ed.* **2019**, *58*, 7035-7039.

[11] T. N. Nguyen, M. Salehi, Q. Van Le, A. Seifitokaldan, C. T. Dinh, *ACS Catal.* **2020**, *10*, 10068-10095.

[12] B. B. Sarma, P. N. Plessow, G. Agostini, P. Concepción, N. Pfänder, L. Kang, F. R. Wang, F. Studt, G. Prieto, *J. Am. Chem. Soc.* **2020**, *142*, 14890-14902.

[13] C. Chu, Q. Zhu, Z. Pan, S. Gupta, D. Huang, Y. Du, S. Weon, Y. Wu, C. Muhich, E. Stavitski, K. Domen, J.-H. Kim, *Proc. Natl. Acad. Sci.* **2020**, *117*, 6376-6382.

[14] T. Sun, S. Mitchell, J. Li, P. Lyu, X. Wu, J. Pérez-Ramírez, J. Lu, *Adv. Mater.* **2021**, *33*, 2003075.

[15] C. Zhao, B.-Q. Li, J.-N. Liu, Q. Zhang, *Angew. Chem. Int. Ed.* **2021**, *60*, 4448-4463.

[16] C. Wan, X. Duan, Y. Huang, *Adv. Energy Mater.* **2020**, *10*, 1903815.

[17] X. F. Lu, B. Y. Xia, S.-Q. Zang, X. W. Lou, *Angew. Chem. Int. Ed.* **2020**, *59*, 4634-4650.

[18] Z. Liang, N. Kong, C. Yang, W. Zhang, H. Zheng, H. Lin, R. Cao, *Angew. Chem. Int. Ed.* **2021**, *60*, 12759-12764.

[19] D. Liu, X. Li, S. Chen, H. Yan, C. Wang, C. Wu, Y. A. Haleem, S. Duan, J. Lu, B. Ge, P. M. Ajayan, Y. Luo, J. Jiang, L. Song, *Nat. Energy* **2019**, *4*, 512–518.

[20] M. Fang, X. Wang, X. Li, Y. Zhu, G. Xiao, J. Feng, X. Jiang, K. Lv, Y. Zhu, W. Lin, *ChemCatChem* **2021**, *13*, 603–609.

[21] N. Yodsin, C. Rungnim, V. Promarak, S. Namuangruk, N. Kungwan, R. Rattanawan, S. Jungsuttiwong, *Phys. Chem. Chem. Phys.* **2018**, *20*, 21194–21203.

[22] J. Yang, S. H. Kim, S. K. Kwak, H. Song, *ACS Appl. Mater. Interfaces* **2017**, *9*, 23302–23308.

[23] Y. Zhou, X. Tao, G. Chen, R. Lu, D. Wang, M.-X. Chen, E. Jin, J. Yang, H.-W. Liang, Y. Zhao, X. Feng, A. Narita, K. Müllen, *Nat. Commun.* **2020**, *11*, 5892.

[24] U. Martinez, S. K. Babu, E. F. Holby, H. T. Chung, X. Yin, P. Zelenay, *Adv. Mater.* **2019**, *31*, 1806545.

[25] G. Zhang, Y. Jia, C. Zhang, X. Xiong, K. Sun, R. Chen, W. Chen, Y. Kuang, L. Zheng, H. Tang, W. Liu, J. Liu, X. Sun, W.-F. Lin, H. Dai, *Energy Environ. Sci.* **2019**, *12*, 1317-1325.

[26] Y.-S. Wei, L. Sun, M. Wang, J. Hong, L. Zou, H. Liu, Y. Wang, M. Zhang, Z. Liu, Y. Li, S. Horike, K. Suenaga, Q. Xu, *Angew. Chem. Int. Ed.* **2020**, *59*, 16013-16022.

[27] Z. Zhang, J. Sun, F. Wang, L. Dai, *Angew. Chem. Int. Ed.* **2018**, *57*, 9038-9043.

[28] J. Li, H. Zhang, W. Samarakoon, W. Shan, D. A. Cullen, S. Karakalos, M. Chen, D. Gu, K. L. More, G. Wang, Z. Feng, Z. Wang, G. Wu, *Angew. Chem. Int. Ed.* **2019**, *58*, 18971-18980.

[29] X. Wang, Y. Jia, X. Mao, D. Liu, W. He, J. Li, J. Liu, X. Yan, J. Chen, L. Song, A. Du, X. Yao, *Adv. Mater.* **2020**, *32*, 2000966.

[30] G. Chen, P. Liu, Z. Liao, F. Sun, Y. He, H. Zhong, T. Zhang, E. Zschech, M. Chen, G. Wu, J. Zhang, X. Feng, *Adv. Mater.* **2020**, *32*, 1907399.

[31] M. Qiao, Y. Wang, Q. Wang, G. Hu, X. Mamat, S. Zhang, S. Wang, *Angew. Chem. Int. Ed.* **2020**, *59*, 2688-2694.

[32] K. Yuan, D. Lützenkirchen-Hecht, L. Li, L. Shuai, Y. Li, R. Cao, M. Qiu, X. Zhuang, M. K. H. Leung, Y. Chen, U. Scherf, *J. Am. Chem. Soc.* **2020**, *142*, 2404-2412.

[33] Y. Chen, Z. Li, Y. Zhu, D. Sun, X. Liu, L. Xu, Y. Tang, *Adv. Mater.* **2019**, *31*, 1806312.

[34] G. Yang, J. Zhu, P. Yuan, Y. Hu, G. Qu, B. Lu, X. Xue, H. Yin, W. Cheng, J. Cheng, W. Xu, J. Li, J. Hu, S. Mu, J.-N. Zhang, *Nat. Commun.* **2021**, *12*, 1734.

[35] X. Zhang, S. Zhang, Y. Yang, L. Wang, Z. Mu, H. Zhu, X. Zhu, H. Xing, H. Xia, B. Huang, J. Li, S. Guo, E. Wang, *Adv. Mater.* **2020**, *32*, 1906905.

[36] X. Wan, X. Liu, Y. Li, R. Yu, L. Zheng, W. Yan, H. Wang, M. Xu, J. Shui, *Nat. Catal.* **2019**, *2*, 259-268.

[37] Z. Song, L. Zhang, K. Doyle-davis, X. Fu, J. Luo, X. Sun, *Adv. Energy Mater.* **2020**, *10*, 2001561.

[38] L. Zhao, Y. Zhang, L.-B. Huang, X.-Z. Liu, Q.-H. Zhang, C. He, Z.-Y. Wu, L.-J. Zhang, J. Wu, W. Yang, L. Gu, J.-S. Hu, L.-J. Wan, *Nat. Commun.* **2019**, *10*, 1278.

[39] J. Fu, R. Liang, G. Liu, A. Yu, Z. Bai, L. Yang, Z. Chen, *Adv. Mater.* **2019**, *31*, 1805230.

[40] C. Tang, Y. Jiao, B. Shi, J.-N. Liu, Z. Xie, X. Chen, Q. Zhang, S.-Z. Qiao, *Angew. Chem. Int. Ed.* **2020**, *59*, 9171-9176.

[41] M. Xiao, L. Gao, Y. Wang, X. Wang, J. Zhu, Z. Jin, C. Liu, H. Chen, G. Li, J. Ge, Q. He, Z. Wu, Z. Chen, W. Xing, *J. Am. Chem. Soc.* **2019**, *141*, 19800-19806.

[42] Y. Mun, S. Lee, K. Kim, S. Kim, S. Lee, J. W. Han, J. Lee, *J. Am. Chem. Soc.* **2019**, *141*, 6254-6262.

[43] F. Li, G.-F. Han, Y. Bu, H.-J. Noh, J.-P. Jeon, T. J. Shin, S.-J. Kim, Y. Wu, H. Y. Jeong, Z. Fu, Y. Lu, J.-B. Baek, *Angew. Chem. Int. Ed.* **2020**, *59*, 23678-23683.

[44] L. Yang, D. Cheng, H. Xu, X. Zeng, X. Wan, J. Shui, Z. Xiang, D. Cao, *Proc. Natl. Acad. Sci.* **2018**, *115*, 6626-6631.

10.1002/anie.202109058

Entry for the Table of Contents

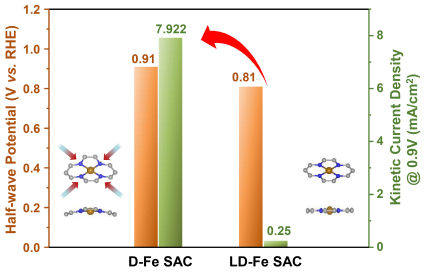

Compressive strain engineering of curved single atomic iron-nitrogen sites could boost the catalytic activity for electrocatalytic oxygen reduction reaction.